npj | computational materials

Article

Published in partnership with the Shanghai Institute of Ceramics of the Chinese Academy of Sciences

https://doi.org/10.1038/s41524-025-01558-w

An NV$^-$ center in magnesium oxide as a spin qubit for hybrid quantum technologies

Check for updates

Vrindaa Somjit[1], Joel Davidsson[2], Yu Jin[3] & Giulia Galli[1,3]

Recent predictions suggest that oxides, such as MgO and CaO, could serve as hosts of spin defects with long coherence times and thus be promising materials for quantum applications. However, in most cases, specific defects have not yet been identified. Here, by using a high-throughput first-principles framework and advanced electronic structure methods, we identify a negatively charged complex between a nitrogen interstitial and a magnesium vacancy in MgO with favorable electronic and optical properties for hybrid quantum technologies. We show that this NV$^-$ center has stable triplet ground and excited states, with singlet shelving states enabling optical initialization and spin-dependent readout. We predict several properties, including absorption, emission, and zero-phonon line energies, as well as zero-field splitting tensor, and hyperfine interaction parameters, which can aid in the experimental identification of this defect. Our calculations show that due to a strong pseudo-Jahn Teller effect and low-frequency phonon modes, the NV$^-$ center in MgO is subject to a substantial vibronic coupling. We discuss design strategies to reduce such coupling and increase the Debye-Waller factor, including the effect of strain and the localization of the defect states. We propose that the favorable properties of the NV$^-$ defect, along with the technological maturity of MgO, could enable hybrid classical-quantum applications, such as spintronic quantum sensors and single qubit gates.

The nitrogen-vacancy center (NV$^-$) in diamond[1] and the divacancy (VV^0) in silicon carbide (SiC)[2] are prototypical spin defects for quantum technologies, including sensing, communication, and computing. A key requirement for these applications is the long coherence time of the spin defect as well as the scalability and integration of the host into current microelectronic platforms. However, the coherence time of defects in diamond and SiC is intrinsically limited by the presence of non-zero nuclear spin isotopes (namely ^{13}C and ^{29}Si, respectively). Additionally, achieving high-yield, scalable fabrication of diamond devices is challenging due to difficulties in etching and polishing diamond[3], and the synthesis of high-quality thin films of a single phase of SiC is a challenge due to its many nearly-degenerate polytypes[4]. Therefore, the identification of new host materials for spin defects is an active field of research.

Recent theoretical work based on cluster correlation expansion simulations predicted that several simple oxide hosts, including calcium oxide (CaO) and magnesium oxide (MgO), could possess long coherence times for spin defects[5]. The work assumed a model spin defect, i.e. a single electron in a dilute nuclear spin bath, and it is still an open question to identify realistic defects in oxide materials. Encouragingly, recent first-principles simulations discovered a Bi complex in CaO, with optical transitions in the telecommunication regime and a coherence time of 4.7 s at clock transitions[6].

In this work, we identify and characterize a promising spin defect in MgO, which has a long and rich history in the microelectronics industry, particularly in spintronics. Magnesium oxide plays a key role in enabling giant tunnel magnetoresistance in magnetic tunnel junctions used in random access memories[7–11]. In addition, MgO tunnel barriers enhance spin injection efficiency from the ferromagnetic source to the semiconducting channel in spin field effect transistors[12]. Although controversial, it has been suggested that MgO might exhibit d^0-ferromagnetism[13–15], which could enable the use of the material as a dilute magnetic semiconductor spin filter in spin transistors. We note that the high dielectric constant of MgO, its low leakage current, and thermal stability make it an ideal material for use as a gate dielectric in thin film transistors[16]. Furthermore, MgO is CMOS-compatible and can be grown in the form of high-quality thin films via a variety of methods[17,18], and it is frequently used as a template layer for

---

[1]Materials Science Division, Argonne National Laboratory, Lemont, IL, USA. [2]Department of Physics, Chemistry and Biology, Linköping University, Linköping, Sweden. [3]Pritzker School of Molecular Engineering and Department of Chemistry, University of Chicago, Chicago, IL, USA.
e-mail: gagalli@uchicago.edu

ferroelectrics[19,20] and superconductors[21]. Thus, identifying spin defects in MgO could open avenues to combine spintronics, ferroelectrics, and quantum information science for the realization of multifunctional, hybrid classical-quantum applications.

Utilizing a high-throughput framework and advanced techniques, including hybrid time-dependent density functional theory (TDDFT) and quantum defect embedding theory (QDET), we identify and characterize a promising spin defect in MgO: an NV^--center. We find that the ground and first excited state of this defect are triplet, with intermediate singlet shelving states; in addition, the NV^- in MgO exhibits a large zero-field splitting (ZFS), and a broad emission side-band in the visible regime. All of these properties together point towards its potential use as a quantum sensor or a spin qubit for quantum technologies. In our study we also report emission spectra, and computed ZFS and hyperfine parameters that may enable the experimental identification of the predicted defect; additionally we analyze the reasons behind the strong vibronic coupling of the electronic states of the NV^- defect with the host MgO lattice, thus providing insights into the engineering of spin defects in oxides.

Results

High-throughput screening of spin defects in MgO

We used a high-throughput technique to screen through thousands of isolated defects and defect complexes and identify favorable spin defect candidates in MgO. The process followed in our study is summarized in Fig. 1. The screening was performed with the ADAQ (Automatic Defect Analysis and Qualification)[22,23] framework, which in turn uses the high-throughput toolkit (*httk*)[24]. This framework has been successfully applied to several host materials, including diamond[25], SiC[26], and CaO[6].

In our search, we considered isolated defects and defect complexes (the latter comprising two neighboring individual defects), including native vacancies and interstitials and their complexes, and substitutional and interstitial defects and defect complexes with *s*- and *p*-elements of the periodic table. We limited our investigation to *s*- and *p*-dopants as we use DFT at the PBE level to screen defects, and we expect that *d*- and *f*-dopants would require the use of DFT+U or hybrid DFT methods, which will be the topic of future investigations, given their higher computational cost. For simplicity, we excluded interstitial-interstitial complexes from the screening. We also restricted our search to complexes with first or second nearest-neighbor defect constituents (i.e. the maximum distance between the two constituent defects in a complex is 3.5 Å), given the cell sizes that are reasonably affordable in our high-throughput procedure, and we included a single type of extrinsic dopant (i.e. we do not consider defect complexes of the type $X_{Mg}Y_{Mg}$, $X_{Mg}Y_O$, $X_{Mg}Int_Y$, X_OInt_Y, where X and Y are different elements substituting the Mg or O site or existing as an interstitial (Int)). Our initial screening yielded 2917 defects, of which 1088 were determined to be on the defect hull–i.e. to have the lowest formation energy per stoichiometry and per Fermi energy[26]. Out of those, we considered the defects with a stable spin triplet ground state (which can thus serve as a two-level system) and which possess a zero-phonon line (ZPL), arriving at the list of the 40 defects tabulated in Supplementary Tables 1 and 2.

We found that 24 of the 40 defects are complexes comprised of second nearest-neighbor defects, which are excluded from further analysis as their experimental synthesis/positioning will likely be challenging. The remaining isolated defects and first nearest-neighbor complexes are shown in Table 1. We find that Ga_O is the only isolated defect with a stable spin triplet ground state; however, we did not consider it since Ga_{Mg} has a much lower formation energy, and thus it is more likely to be formed when Ga is implanted in MgO. Several complexes listed in Table 1 are of the type X_OVac_{Mg}, where the dopant X (X = B, I, Sb, Bi) lies between the magnesium and oxygen vacancy sites. This class of defects was first identified in CaO, where the Bi dopant has been proposed to be suitable for quantum applications due to the presence of a clock transition[6]. These defects were excluded from the present study, as we expect them to have similar optical and spin properties as those in CaO, including, unfortunately, a low Debye-Waller factor. Note that in MgO, the B_OVac_{Mg} defect is stable, unlike in CaO, but it has a higher formation energy (by 7 eV) than those discussed below. Further, several complexes of the type $X_{Mg}X_O$, where X = B, Al, Ga, In, Tl are stable, with a detectable ZPL; however they are likely difficult to synthesize due to the slow diffusion of substitutional impurities[25] and high formation energies (due to cations substituting the oxygen site), and hence they were not further analyzed. Interestingly, our search identified additional five defects with a spin triplet ground state and possessing a ZPL; but they all consist of anions substituting the magnesium site and/or cations substituting the oxygen site, and thus they will likely have large formation energies and be challenging to synthesize (see Supplementary Note 1).

Finally, we are left with the defect Int_NVac_{Mg}, comprising a nitrogen interstitial next to a magnesium vacancy; it is similar to the NV^- in diamond, which, however, is formed by a nitrogen substitutional, instead of interstitial, next to a carbon vacancy. The synthesis of Int_NVac_{Mg} is expected to be straightforward, since interstitials generally have low diffusion barriers in MgO[27,28]. Moreover, nitrogen doping of MgO via, e.g. molecular beam epitaxy and implantation has been reported in the literature[29–34]. Thus, we choose to investigate the Int_NVac_{Mg} defect (referred to as NV^- hereafter) for the remainder of our study.

We note that several previous studies have investigated nitrogen dopants in MgO using first-principles methods[35–41], addressing the

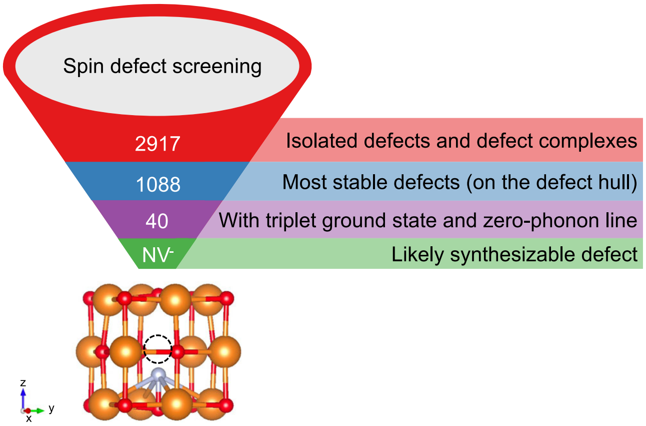

Fig. 1 | High-throughput screening of spin defects in MgO. Schematic of the workflow, which includes creation of isolated defects and complexes including *s*- and *p*-dopants and intrinsic defects, which are screened based on stability, presence of a spin triplet ground state and zero-phonon line, and synthesizability (see text), leading to the identification of an NV^- center in MgO (shown in inset).

Table 1 | Isolated defects and first nearest-neighbors complexes on the defect hull, with spin triplet ground state and zero-phonon line (ZPL), as obtained from the screening process of Fig. 1, using the PBE functional

Defect Type	Defect	Charge	ZPL [eV]
X_OVac_{Mg}	B_OVac_{Mg}	−1	0.5
	I_OVac_{Mg}	1	0.74
	Sb_OVac_{Mg}	−1	3.1
	Bi_OVac_{Mg}	−1	0.7
$X_{Mg}X_O$	$B_{Mg}B_O$	0	1.39
	$Al_{Mg}Al_O$	0	0.68
	$Ga_{Mg}Ga_O$	0	1.29
	$In_{Mg}In_O$	0	0.98
	$Tl_{Mg}Tl_O$	0	1.81
X_O	Ga_O	−1	4.19
Int_XVac_{Mg}	Int_NVac_{Mg}	−1	2.19

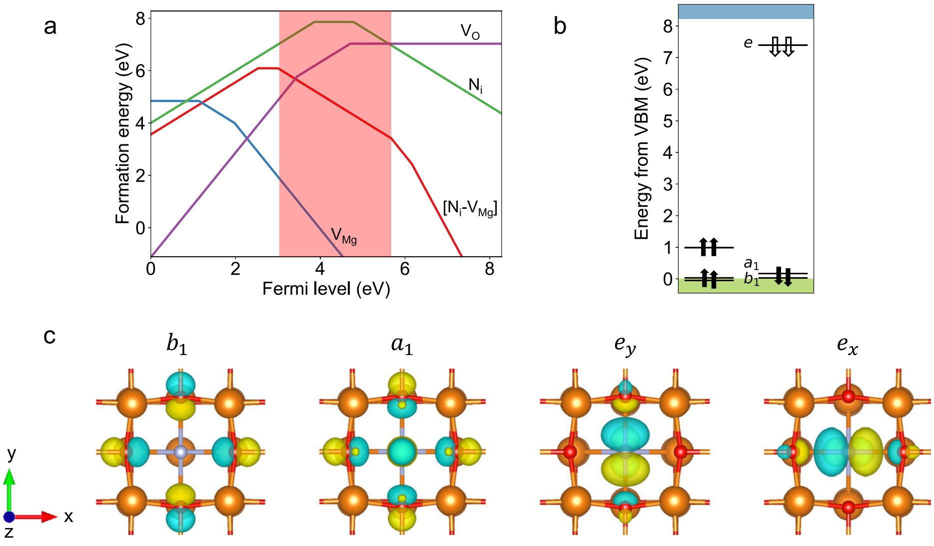

Fig. 2 | Ground state properties of the NV⁻ center in MgO computed with hybrid DFT (see text). **a** Formation energies of different point defects in MgO under oxygen- and nitrogen-rich conditions as a function of the Fermi level: V_O, N_i, V_{Mg} and $[N_i - V_{Mg}]$ denote an oxygen vacancy, nitrogen interstitial, magnesium vacancy, and a nitrogen interstitial-magnesium vacancy complex, respectively. The shaded area shows the stability region for the NV⁻ defect. **b** Defect level diagram of the NV⁻ defect with the single-particle defect levels labeled according to the irreducible representation of the C_{4v} point group. Solid (empty) arrows denote occupied (unoccupied) defect levels. In the minority spin channel, the b_1, a_1, and e orbitals are 0.03 eV, 0.17 eV, and 7.39 eV above the VBM, respectively. **c** Iso-surfaces (level: 0.003 e/Å^3) of the square moduli of the Kohn-Sham orbitals in the spin down channel. Orange, red, and gray spheres represent magnesium, oxygen, and nitrogen atoms, respectively. The viewing direction is along the C_4 axis.

possibility of d^0-magnetism in MgO and its application as a dilute magnetic semiconductor for spintronic devices. These studies explored the effect of nitrogen substituting the oxygen site[35,37–41], nitrogen interstitials[39], and nitrogen dimers[36]. However, they did not investigate the NV⁻ complex and did not report any excited state properties relevant to quantum applications.

Ground state properties using hybrid DFT

We investigated the ground state properties of the NV⁻ center in MgO using density functional theory (DFT) with the dielectric-dependent hybrid (DDH) exchange-correlation functional[42]. The inverse of the experimental macroscopic dielectric constant $\epsilon_\infty = 2.96$ was used as the fraction of exact exchange, i.e. $\alpha = 0.34$[42,43]. The DDH functional is able to recover the experimental band gap at 0 K accurately (after accounting for zero-point motion renormalization effects), unlike semi-local functionals like PBE, which underestimate the bandgap (see Supplementary Table 3 for a comparison between the band gaps obtained using PBE, DDH, and experiment).

As shown in the inset of Fig. 1, the NV⁻ defect in MgO has C_{4v} symmetry in the ground state, with a nitrogen atom present at the bond-center interstitial site, bonded to four neighboring magnesium atoms ($d_{N-Mg} = 2.49$ Å) and an oxygen atom ($d_{N-O} = 1.33$ Å), with a nearest neighbor magnesium vacancy and an additional electron. The fourfold rotation axis (C_4) is along the N-O bond in the < 001 > direction. We plot the defect formation energies of relevant defects under O_2-rich, N_2-rich conditions as a function of the Fermi level in Fig. 2a. We see that the NV⁻ is stable within the bandgap and therefore, may be experimentally realizable. Further, we expect that NV⁻ will be compensated by positively charged oxygen vacancies. Note that the Fermi energy may be pinned at 2.3 eV above the valence band maximum (VBM) due to compensating native defects (magnesium and oxygen vacancies) under high-temperature equilibrium growth conditions. One strategy to move the equilibrium Fermi level into the stability region of the NV⁻ defect could be to n-dope MgO during growth, for example, with Al^{3+}[44] or Fe^{3+}[45]. This would have to be done carefully to avoid the introduction of additional optically active defects and a high concentration of spinful nuclei into the sample. However, sample preparation techniques could be designed to circumvent the requirement of n-type doping. Specifically, sample preparation typically involves high-temperature growth in a nitrogen-rich environment, followed by a cooling down process where the nitrogen flux is turned off, thereby fixing the concentration of nitrogen in the sample. Under these low temperature conditions and high nitrogen concentrations, where the contribution from configurational entropy is low, binding energy effects will be predominant[46]; hence they will promote the formation of the NV⁻ complex, especially given its high binding energy (E_b = 2.86 eV, calculated as $E_b = E_f(V_{Mg}^{2-}) + E_f(N_i^{1+}) - E_f(NV^-)$; V_{Mg}^{2-} and N_i^{1+} denote the doubly-negatively charge magnesium vacancy and the singly-positively charged nitrogen interstitial). In general, the defects formed will strongly depend on the sample preparation techniques (for example, nitrogen incorporation during growth vs. implantation). Figure 2a is indicative of the fact that the NV⁻ defect can be formed in MgO by optimizing sample preparation conditions, as it is stable within the bandgap. Additionally, we checked for the possibility of the nitrogen interstitial recombining with the magnesium vacancy to form a substitutional nitrogen defect on the magnesium site. We found that the NV⁻ defect is the preferred configuration; this result can be understood from a molecular orbital analysis, presented in Supplementary Note 3. Finally, we also computed the barrier for the nitrogen interstitial to migrate to other interstitial sites around the vacancy (see Supplementary Note 4). The computed barrier is high (≈1.37 eV), thus, once formed, the NV⁻ defect is expected to be stable against annealing.

The defect level diagram of the NV⁻ center obtained using the DDH functional is shown in Fig. 2b. We see that the ground state is a spin triplet, with four isolated defect states present within the bandgap of MgO: one b_1, one a_1, and two degenerate e orbitals. Figure 2c shows the iso-surfaces of the square moduli of the Kohn-Sham orbitals of the four defect states in the spin down channel as viewed along the C_4 axis. We find that the b_1 and a_1 defect states near the valence band maximum (VBM) consist of O $2p$ orbitals arising from the presence of the magnesium vacancy, and the degenerate e defect states consist of π-orbitals (π_{px}, π_{py}) from the N-O bond. In fact, the additional electron in this complex localizes on the N-O bond in one of the π-orbitals. The separation of the occupied and unoccupied defect states from each other as well as from the valence and conduction bands of MgO indicate that optical transitions to prepare and measure the qubit state are possible.

To aid in the experimental identification of the NV⁻, for example via electron paramagnetic resonance (EPR) or magnetic circular dichroism experiments, we calculated the zero-field splitting (ZFS) tensor and the hyperfine parameters. A sufficiently large ZFS is required to isolate the $m_s = \pm 1$ and $m_s = 0$ sublevels of the ground state triplet at zero magnetic field, allowing for the controllable preparation of the spin qubit. As expected from the C_{4v} symmetry of this defect, the transverse E value is 0. Our computed axial D component of the ZFS tensor is 38.48 (46.38) GHz at the PBE (DDH) level. This value represents the energetic separation between the $m_s = \pm 1$ and $m_s = 0$ sublevels, indicating that the defect can be initialized conveniently in the $m_s = 0$ sublevel. Furthermore, the computed value of D is favorable to prevent excitations from the $m_s = 0$ to $m_s = \pm 1$ sublevel, thus protecting the qubit from decoherence, while still being measurable via traditional microwave EPR experiments (instead of requiring a high-frequency EPR setup, for example). Note that this value of ZFS is much larger than that reported for defect qubits in diamond, SiC, and AlN (where many spin defects have ZFS smaller than 5 GHz[47]), but it is of the same order of magnitude as that of the Ti_{VV} center in 2D h-BN (19.4 GHz)[48] and SiV in diamond (46 GHz)[49], and lower than that reported for other qubit systems, e.g. single molecule magnets (for which ZFS can reach up to 13000 GHz)[50].

EPR measurements also yield hyperfine parameters, which describe the coupling between the electron spins and nuclear spins. The NV^- defect in MgO has the following nuclear spins: ^{14}N (I = 1, 99.63%), ^{25}Mg (I = 2.5, 10%), and ^{17}O (I = 2.5, 0.038%), and the principal values of its hyperfine tensors are given in Table 2. Pesci et al.[39] investigated nitrogen interstitials in MgO and found that electrons localize on the π-orbitals around the N-O bond, consistent with our findings. Interestingly, their reported hyperfine parameters for substitutional nitrogen on the oxygen site and interstitial nitrogen are different from our calculated values for the NV^- defect (see Supplementary Table 4 for a comparison), indicating that the latter might be experimentally distinguishable from other nitrogen defects in the MgO lattice, using EPR.

Overall, the ground state properties of the NV^- in MgO indicate that this defect is stable over a large energy range within the band gap of the host and thus, should be experimentally realizable. It has a spin triplet ground state with isolated occupied and unoccupied levels, pointing to the possibility of optical transitions to prepare and measure a qubit state. The computed ZFS tensor shows that a sufficiently large separation between spin sublevels is present, and that initialization in the $m_s = 0$ sublevel should be realizable experimentally. Further, the computed hyperfine parameters indicate that the NV^- center is expected to be distinguishable from other nitrogen defects in MgO.

Table 2 | Computed principal values of the hyperfine tensors (A) at the PBE level of theory (in MHz) for the NV^- defect in MgO

Atom	A_{xx}	A_{yy}	A_{zz}
N atom	43.58	43.59	−87.17
O atom bonded to N	−27.86	−27.89	55.76
Mg atoms nearest-neighbor to N	0.27	0.47	−0.74
O atoms nearest-neighbor to magnesium vacancy	11.07	12.30	−23.37

Excited state properties using hybrid TDDFT

We now turn to investigate the excited state properties of the NV^- center using time-dependent density functional theory (TDDFT) with the DDH functional, as implemented in the WEST code[51]. We used spin-conserving and spin-flip TDDFT-DDH to investigate triplet and singlet excited states, respectively. The relaxed structure of the triplet ground state and first excited triplet state (obtained using DDH and TDDFT-DDH, respectively) are shown in Fig. 3a.

Figure 3b plots the vertical excitation energies of multiple low-lying singlet and triplet states, as obtained from TDDFT-DDH. The first excited state triplet ^3E is about 5 eV above the triplet ground state ($^3A_2$), with additional excited state triplets (^3E) close in energy. Additionally, we find three singlet states ($^1A_1$, $^1B_1$, $^1B_2$) within the energy range of the first triplet excitation, indicating that an optical initialization cycle, similar to that of the NV^- center in diamond, may be possible.

We also characterized the electronic excitations using quantum defect embedding theory (QDET)[52–54] and compared the results with those of TDDFT-DDH. In QDET, we define an active space that consists of single-particle orbitals involved in the excitations of interest and a many-body effective Hamiltonian acting on this space, which includes the influence of the environment surrounding the defect. The electronic structure of the environment is described at the G_0W_0 level of theory, enabling an exact correction for the double-counting terms. For the NV^-, we chose an active space consisting of the four localized defect states within the band gap (b_1, a_1, e_x, e_y), as well as of defect states close to the valence band maximum. The eigenstates of the effective Hamiltonian are determined exactly using the full configuration interaction method, yielding the many-body level diagram shown in Fig. 3b. We see that the trends in excited state energies using TDDFT-DDH and QDET are the same. The minor differences in absolute energy values between the two methods could arise due to the absence of double excitations in TDDFT and/or a limited active space in QDET. Work is ongoing to understand the performance of QDET on a broader class of defects and hosts, which will help clarify the reasons behind the difference

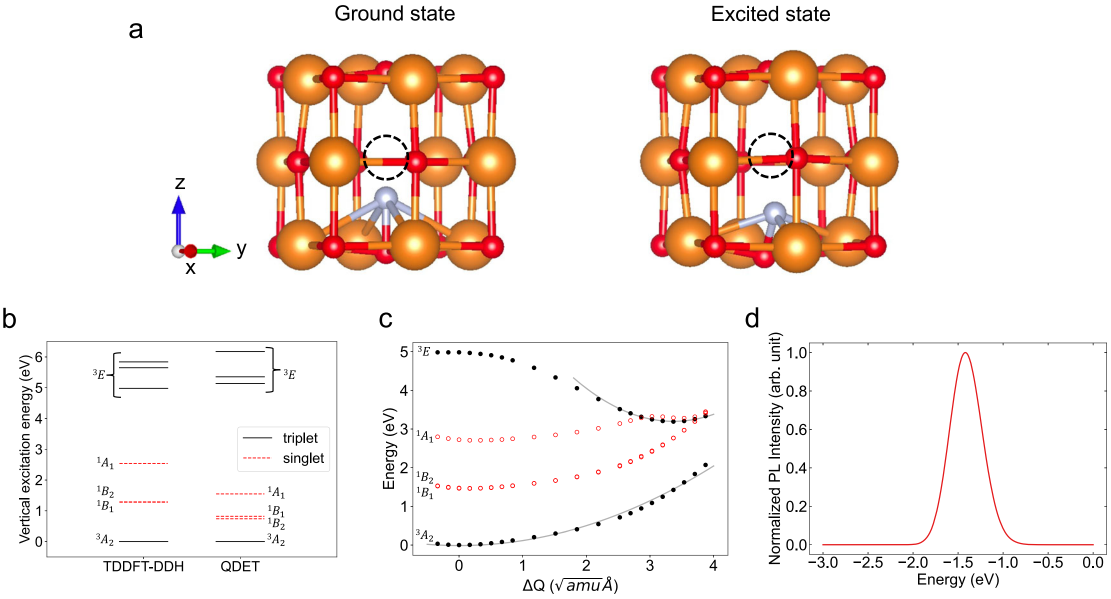

Fig. 3 | Excited state properties of the NV^- center in MgO. a Optimized structures of the ground state $^3A_2$ and first excited ^3E state obtained using DFT-DDH and TDDFT-DDH, respectively. Black dotted circle denotes the magnesium vacancy. **b** Many-body level structure obtained using TDDFT-DDH and quantum defect embedding theory (QDET). **c** One-dimensional configurational coordinate diagram constructed between the optimized structures of the $^3A_2$ ground state and first ^3E excited state. The points denote energies obtained at each ground state (excited state) configuration using single-point DDH (TDDFT-DDH) calculations. Solid lines show a quadratic fit. **d** Calculated emission (photo-luminescence, PL) spectrum at 300 K aligned with respect to the zero-phonon line.

Table 3 | Optical properties of the NV$^-$ defect in MgO obtained using TDDFT-DDH (see text)

Property	NV$^-$ MgO	NV$^-$ diamond	VV^0 4H-SiC
Absorption (eV)	4.98	2.21[106]	1.18, 1.27[107]
ZPL (eV)	3.19	1.96[106]	1.13, 1.21[107]
Emission (eV)	1.76	1.74[106]	1.09, 1.18[107]
ΔR (Å)	0.84	0.18[58]	0.16, 0.18[22]
ΔQ (amu$^{0.5}$ Å)	3.37	0.62[106]	0.60, 0.74[22]

The values for diamond and SiC are taken from the literature and are obtained using the HSE functional. The two values for SiC are for the *hh* axial VV^0 and *hk* basal VV^0, respectively. *ZPL* : zero-phonon line, ΔR : total displacement between the excited and ground state structures, ΔQ : mass-weighted displacement between the excited and ground state structures.

between the TDDFT and QDET results; detailed comparisons will be reported elsewhere. For the problem at hand here, the important point is that the order of multi-reference states obtained with TDDFT and QDET is the same.

Having determined the vertical excitation energies, we proceeded to relax the structure in the first excited triplet (^3E) state using TDDFT-DDH with analytical forces[51] (see Fig. 3a). A decomposition of the many-body state shows that the $a_1 \rightarrow e$ excitations are dominant. We note that in the relaxed geometry of the excited state, the symmetry is reduced to C_1, with d_{N-Mg} = 1.98–2.86 Å and d_{N-O} = 1.37 Å. We find four equivalent minima, with the N-O bond tilted along the $+x$, $-x$, $+y$, $-y$ directions, consistent with the C_{4v} symmetry of the ground state. Table 3 lists the absorption, zero phonon line (ZPL), and emission energies of the NV$^-$ in MgO (calculated under the Franck-Condon approximation) and compares it with that of the NV$^-$ center in diamond and the VV^0 in silicon carbide. In MgO, the absorption and ZPL of the NV$^-$ center are in the ultraviolet (UV) range whereas the emission is in the visible range, highlighting a large Stokes shift.

A large Stokes shift implies that a large number of phonons are involved in the emission process, which could lower the intensity of the ZPL relative to the rest of the emission spectrum, thus yielding an unfavorable Debye-Waller factor (DWF). The average number of phonons emitted during an electronic transition is called the Huang-Rhys factor (HRF, denoted as S) and is given by ref. 55

$$S = \frac{\frac{1}{2}\Delta Q^2 \omega_{eff}^2}{\hbar\omega_{eff}} \tag{1}$$

where ω_{eff} is an effective phonon frequency and ΔQ a mass-weighted displacement. The latter is calculated as

$$\Delta Q = \left(\sum_{\alpha=1}^{N} \sum_{i=x,y,z} M_\alpha \Delta R_{\alpha i}^2 \right)^{1/2} \tag{2}$$

where M_α = mass of atom α, $\Delta R_{\alpha i}$ = displacement of atom α between the excited state and ground state equilibrium structures in the ith direction). Not surprisingly, given the large Stokes shift, we find that the ΔQ of the NV$^-$ is large (see Table 3), indicating a strong electron-phonon coupling[55,56].

We calculated ω_{eff}, and therefore, the HRF S, by constructing a one-dimensional configuration coordinate diagram (CCD) along the direction connecting the relaxed $^3A_2$ ground and ^3E excited state structures[57,58] (geometries optimized using DDH and TDDFT-DDH, respectively), as shown in Fig. 3c. By fitting a quadratic function around the points near the respective minima, we obtain the effective phonon frequencies of the ground and excited states to be $\hbar\omega_g$ = 32.79 meV and $\hbar\omega_e$ = 61.77 meV respectively. Using $\hbar\omega_g$ and ΔQ, we obtain the HRF for emission as S = 44.49, which is again indicative of a strong electron-phonon coupling[55], as expected. Such a large HRF leads to a negligible Debye-Waller factor (DWF $\simeq e^{-S} \approx 10^{-20}$), as a majority of the photons contribute to the emission side band instead of the ZPL. Thus, the ZPL will likely be undetectable, rendering the defect unsuitable as a single photon emitter (for example, for quantum communication applications). However, the defect's triplet ground state, large ZFS, and many-body level structure may make it suitable for quantum sensing, computing, or transduction, by enabling optical initialization and spin-selective photo-luminescence. In fact, the possibility of optical initialization and readout is further highlighted from the CCD of the singlet excited states plotted in Fig. 3c. We see that at the ^3E minimum, $^1A_1$ is nearly degenerate with ^3E, and $^1B_1$ and $^1B_2$ are lower in energy than the ^3E state. Thus, despite the large ΔQ in this system, the singlet states' potential energy surfaces do not cross that of the triplet ^3E excited state (or are nearly degenerate with the ^3E minimum, as in the case for $^1A_1$), indicating that optical initialization and spin-selective photoluminescence via inter-system crossing (ISC) may be possible. While the rates for these transitions would need to be calculated, this is an important prerequisite for the possibility of optical initialization and readout, as further discussed below. Finally, nanostructuring or the additional presence of extended defects can be used to lower the HRF and therefore increase the intensity of the ZPL, as explored in SiC[59].

Using $\hbar\omega_g$, $\hbar\omega_e$, and ΔQ, we show the emission spectrum of the NV$^-$ in Fig. 3d, which is nearly a Gaussian with a peak at the Franck-Condon energy of 1.43 eV, and a line-width of 420 meV. The emission spectrum thus lies in the visible red-infrared region, making it easy to detect. Moreover, a broad line-width is advantageous as it would allow multiple frequency filters to be used (for example, to filter out emissions from an underlying substrate) while retaining a significant fraction of the emission spectrum to be employed for detection. The radiative lifetime is 23 μs, calculated as the inverse of the radiative rate $\Gamma_R = \frac{n_r \mu_{\mathrm{em}}^2 (E_{\mathrm{em}})^3}{3\pi\epsilon_0 c^3 \hbar^4}$, where n_r is the refractive index of MgO (1.73), μ_{em} is the transition dipole moment for emission (0.035 e Å) calculated using TDDFT-DDH, and E_{em} is the emission energy calculated using TDDFT-DDH (1.76 eV). This value is three orders of magnitude larger than those computed for the NV$^-$ in diamond[60] and VV^0 in SiC[61], but is similar to those computed for spin defects in 2D transition metal dichalcogenides[62]. While it would be preferable to have a shorter radiative lifetime, the non-radiative lifetime is likely longer, as the ^3E and $^3A_2$ potential energy surfaces cross only at large barrier energies, and non-radiative rates are typically low for defects with transition energies larger than 1.5 eV[63]. Moreover, we note than the predicted coherence time T_2 for an electron spin defect in MgO is 600 μs[5], thus, the spin state could still be retained during optical initialization and readout. Nonetheless, cavity enhancement may be required due to other competing processes like inter-system crossing. Cavity enhancement of over 1000 has recently been reported for transitions in Er^{3+}-doped MgO[64]. This result points to the encouraging possibility of cavity enhancement of the transitions in the NV$^-$ center in MgO as well.

To summarize the computed excited state properties of the NV$^-$ in MgO, we find the presence of triplet excited and singlet shelving states, pointing at the possibility of an optical initialization cycle and spin-selective photo-luminescence. Further, our results show that the absorption and ZPL energies are in the UV range, whereas the emission energy is in the visible (red) range. The visible emission energy, together with the computed broad emission side-band, is a convenient feature for experimental detection in applications such as quantum sensing and transduction. We also find a large ΔQ and related Stokes shift, large HRF, and low DWF, indicating strong vibronic coupling. Identifying the reason behind this strong coupling is key to determining engineering strategies that can mitigate it, and to enhance our understanding of oxides as hosts for spin defects. We explore this in further detail below.

Vibronic analysis

According to the character table of the C_{4v} point group (see Supplementary Table 5), the E electronic states can couple linearly to the a_1, a_2, b_1, b_2 phonon modes, and to e phonon modes via higher (even) order coupling. However, only the b_1, b_2, and e phonon modes can reduce the symmetry of the defect. Given that the C_{4v} symmetry is reduced to C_1 in the optimized geometry of the first excited ^3E state, e-phonon modes are expected to be predominantly coupled to the electronic states (b_1 and b_2 modes would have

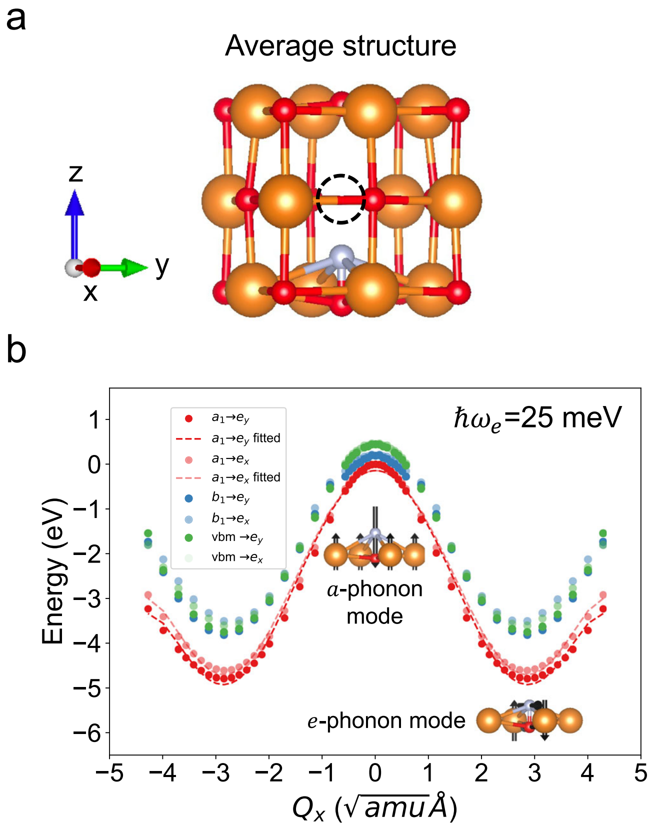

Fig. 4 | Analysis of vibronic coupling. a Average structure of the four equivalent excited state minima of the NV^- center in MgO. **b** One dimensional configurational coordinate diagram along e_x-phonon mode, showing the first three ^3E excited states. The points denote energies obtained at each configuration using single-point TDDFT-DDH calculations. The adiabatic potential energy surface of the first ^3E-excited state is shown by the dashed lines. The predominant phonon modes involved in the average structure and the excited state structure are shown as insets. The displacement vectors of phonon modes are scaled up for clarity.

reduced the symmetry to C_2 and C_{2v}, respectively). To verify that indeed the e phonon modes are responsible for the observed symmetry-breaking in the first excited ^3E state, we calculated the Mg, O, and N displacements between the average structure of the four equivalent minima (shown in Fig. 4a) and the optimized geometry of the excited state (shown in Fig. 3a). The average structure is symmetrical and the displacement between the average geometry and that of the relaxed excited state geometry may be used to understand the predominant symmetry-breaking mode. We found that the symmetry-breaking displacements are predominantly due to the e-phonon mode (see Supplementary Note 6 and insets of Fig. 4b).

Thus, using the projections of the eigenvectors of the e-phonon modes as the collective variables (i.e. along x and y axes), and using the averaged structure as a reference geometry (since the symmetric a_1-phonon modes are not Jahn-Teller or pseudo-Jahn Teller active), we built a CCD of the first three excited states using TDDFT-DDH. The CCD along the e_x-phonon mode, identical to the one along the e_y mode, is shown in Fig. 4b. Interestingly, we observe the presence of close-spaced excited states with negative curvature at $\Delta Q = 0$, separated by only ~0.2 eV, indicating that they likely interact strongly via the pseudo-Jahn Teller (pJT) effect. These excited states originate from excitations of the form $a_1 \rightarrow e$, $b_1 \rightarrow e$, and $VBM \rightarrow e$. The close-spaced excited states found here are ^3E-states, similar to those seen in spin-conserving TDDFT-DDH and QDET calculations of the vertical excitation energies of the ground state structure, shown in Fig. 3b.

To quantify the coupling between the various states, we fit an adiabatic potential energy surface (APES) to the first excited state CCD, which yields an effective phonon frequency of the e-phonon mode and the vibronic coupling constants. Specifically, we solve a $(E+E)\otimes e$ Hamiltonian, which accounts for Jahn-Teller (JT) coupling within each ^3E state and pseudo-Jahn Teller (pJT) coupling between two excited ^3E states. We used an adiabatic-to-diabatic transformation of the potential energy matrix and built an effective Hamiltonian that includes coupling constants for JT and pJT effects[65,66]. We then fit the eigenvalues of the Hamiltonian to the TDDFT-DDH energy values along the CCD of the first excited state to obtain the parameters of the energy matrix. The details of the derivation are given in Supplementary Note 7. The APES of the first excited ^3E state along the e-phonon mode is shown in Fig. 4b, from which we obtained the effective phonon frequency of the e-phonon mode to be 25 meV, and the vibronic coupling parameters to be 20–500 meV. We also found that the pJT effect is more pronounced than the JT effect: including the JT coupling parameters did not reduce the fitting error of the APES (see Supplementary Note 7 for more details). The pJT stabilization energy is large (~5 eV). These vibronic coupling parameters are far larger than those of the NV^- in diamond (in which vibronic coupling is around 120 meV[67]), and the effective phonon frequency is far lower than that of the NV^- in diamond (effective phonon frequency of the latter is around 60 meV[67]). The large pJT stabilization energy and low effective phonon frequencies satisfy the condition for strong vibronic coupling, given as[56]

$$\frac{E_{PJT}}{\hbar\omega_{eff}} \gg 1 \tag{3}$$

Thus, from our vibronic coupling analysis, we find that the strong vibronic coupling of the first excited state to the e phonon modes is due to a large pJT stabilization energy and low effective phonon frequencies. In turn, this strong coupling gives rise to a large ΔQ and then to a large Stokes shift and HRF, and to a low DWF.

We end this section by briefly mentioning that the strong vibronic coupling could indicate a strong spin-phonon coupling, which might lead to a reduction in the spin relaxation time T_1. While a spin-phonon coupling analysis is beyond the scope of this study, we did calculate the phonon modes for the NV^- defect in the ground state, as discussed in Supplementary Note 8. We find that the modes are largely localized near the NV^- defect and have energies that generally exceed its ZFS. Thus, the spin relaxation time T_1 might be limited by slower two-phonon processes as opposed to fast one-phonon direct and Orbach relaxation mechanisms. Having predominantly two-phonon processes would be desirable for an optimal value of the defect's T_1.

Engineering strategies to reduce vibronic coupling and increase DWF

Having obtained insight into the reasons behind the strong vibronic coupling of the NV^- center in MgO, we now discuss potential strategies to reduce such coupling, and therefore, the large ΔQ, and potentially increase the DWF.

As our first strategy, we explored the effect of strain on the optical properties of the NV^-. Strain has been reported to change the alignment of spins of the NV^- in diamond[68] and stabilize the spin triplet state in AlN[69]. We considered biaxial strain, since under thin film growth conditions, MgO will be epitaxially strained to match the lattice constants of the substrate, while relaxing its geometry along the perpendicular direction. Estimates using ΔSCF-PBE (i.e. differences of total energies computed with different occupation numbers, see Supplementary Note 9) revealed that biaxial compressive strain in the xy-plane reduced the ΔQ while retaining the degeneracy of the e-levels. Hence, we investigated two different biaxial compressive strain levels: 1% and 4%, and optimized the geometries of the NV^- structure in its ground and first excited state using DFT-DDH and TDDFT-DDH, respectively. Our chosen strain values are experimentally representative, as MgO thin films can be epitaxially grown up to thicknesses of ~ 1 nm with a biaxial compressive strain of 4% on substrates like Fe[70] and Ag[71]. Hereafter, 'strain' refers to 'biaxial compressive strain in the xy-plane'.

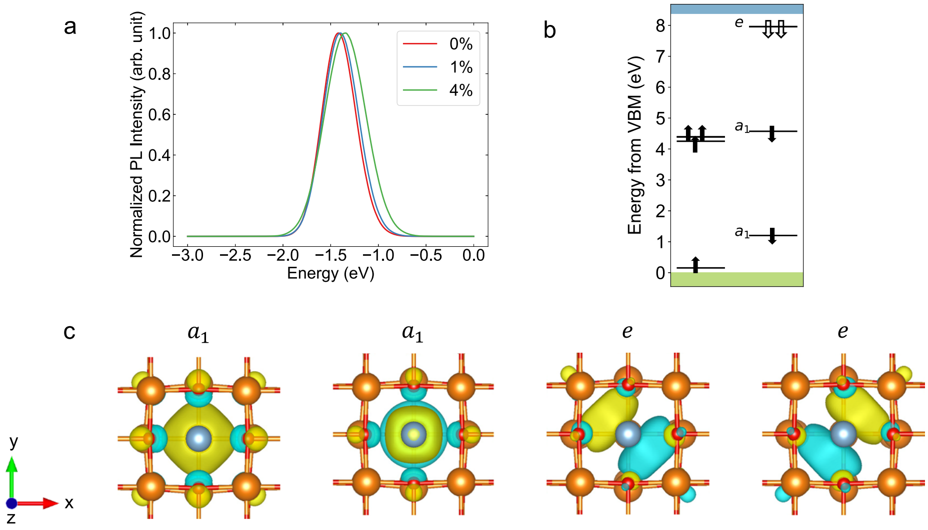

Fig. 5 | Engineering strategies to reduce vibronic coupling. a Calculated emission (photo-luminescence, PL) spectrum of the NV$^-$ defect in MgO at 300 K as a function of biaxial compressive strain, aligned with respect to the zero-phonon line. **b** Defect level diagram obtained using the DDH functional for the $\mathrm{Al_{Mg}-Al_O}$ defect complex in MgO with the single-particle defect levels labeled according to the irreducible representation of the C_{4v} point group. Solid (empty) arrows denote occupied (empty) defect levels. **c** Iso-surfaces (level: 0.0007 e/Å^3) of the square moduli of the Kohn-Sham orbitals in the spin down channel for the $\mathrm{Al_{Mg}-Al_O}$ defect complex.

Notably, we find that as strain increases (0 %, 1%, 4%), there is a reduction in ΔQ (3.37, 3.15, 2.78 amu$^{0.5}$ Å), indicating a decrease in vibronic coupling.

To check if this reduction in ΔQ leads to a reduced HRF and increased DWF, we followed the same strategy as described previously. We constructed a one-dimensional CCD along the direction connecting the optimized geometries in the ground and excited state using TDDFT-DDH and fit a quadratic function around the points in proximity of the respective minima. In this way, we obtained effective phonon frequencies of the ground and excited states under the different strain conditions, which we used to calculate the HRF. We find that strain decreases the HRF from 44.49 (unstrained case) to 41.36 (1% strained case) and 36.23 (4% strained case). This results in an increase in the DWF by 4 and 7 orders of magnitude respectively; however, unfortunately the ZPL would still be undetectable, as the DWF of the unstrained system is extremely low ($\approx 10^{-20}$).

The emission spectra at different strain conditions are shown in Fig. 5a, calculated with the same method of Fig. 3d, i.e, by using the respective $\hbar\omega_g$, $\hbar\omega_e$, and ΔQ. We once again see that the spectra are nearly Gaussian, with a mean around the respective Franck-Condon energies. The reduction in HRF is manifested as a slight red-shift in the mean of the emission spectrum.

Overall we find that strain can reduce the ΔQ and HRF, and therefore the vibronic coupling, thus increasing the DWF of the NV$^-$ defect in MgO by orders of magnitude; however, since the DWF of the unstrained system is negligible, the impact of strain on the DWF value is not sufficient to obtain a substantial increase.

As our second strategy, we explored the role of the defect electronic structure on ΔQ (and, therefore, vibronic coupling and DWF), by investigating another promising defect found in the MgO ADAQ database: the $\mathrm{Al_{Mg}-Al_O}$ defect complex. It has the the lowest ΔQ among the 20 nearest-neighbor defect complexes with a spin triplet ground state and ZPL, the latter in the near-telecom regime. In contrast to the NV$^-$ center, which consists of an interstitial-vacancy complex, the $\mathrm{Al_{Mg}-Al_O}$ complex consists of two substitutional impurities, and its analysis gives us insight into a different class of defects. Note however that unfortunately, the $\mathrm{Al_{Mg}-Al_O}$ complex has a very high formation energy (around 11 eV); thus, its experimental realization might be challenging.

Figure 5b shows the defect level diagram and Fig. 5c shows the iso-surfaces of the square moduli of the Kohn-Sham orbitals of the four defect states in the minority spin channel. We note two key differences in the electronic structure of this defect, compared to the NV$^-$ center. First, there is a large separation between the highest and next-highest occupied defect levels in the minority spin channel of $\mathrm{Al_{Mg}-Al_O}$, unlike the NV$^-$, where the a_1 and b_1 defect orbitals lie very close in energy to each other and to the valence band maximum. The increased energetic separation between the Kohn-Sham orbitals could lead to an increased separation between the low-lying excited states, thereby minimizing pJT effects and lowering the vibronic coupling, and leading to a lower value of ΔQ. In fact, the energy separation between the vertical excitation energies of the first two ^3E states (calculated using TDDFT-DDH) is 1.64 eV for the $\mathrm{Al_{Mg}-Al_O}$ defect, compared to 0.67 eV for the NV$^-$ center (see Fig. 3a). Thus, a strong vibronic coupling via the pJT effect is unlikely to occur in $\mathrm{Al_{Mg}-Al_O}$. Second, the occupied and unoccupied Kohn-Sham orbitals of the minority spin channel (which are involved in the excitation) are localized around the same Al atom in $\mathrm{Al_{Mg}-Al_O}$. This is unlike in NV$^-$, where the occupied defect orbitals localize near the Mg vacancy and the unoccupied defect orbitals localize on the N-O bond. Moreover, in the case of NV$^-$, the excitation is from the O 2*p* orbitals of the Mg vacancy to the π-orbital on the N-O bond. Instead in $\mathrm{Al_{Mg}-Al_O}$, the excitation is between similar π-type orbitals on the same Al atom. Since a large change in the charge distribution of the defect electrons during an optical transition usually leads to a large HRF[55], the comparatively low ΔQ of the $\mathrm{Al_{Mg}-Al_O}$ defect complex may originate, at least in part, from the localization of the orbitals involved in the transition around the same atom.

Thus, spin defects in oxides comprising substitutional impurities may lead to lower values of ΔQ and an increased DWF. These defects are expected to possess a large separation between Kohn-Sham defect levels (as compared to those with native defects such as cation vacancies) and result in the localization of the occupied and unoccupied defect states on the substitutional dopant itself. In this respect, *d*- or *f*-dopants might be promising, given that they likely substitute the cation site, and involve intra-shell *d*-*d* or *f*-*f* transitions, which might not experience a strong vibronic coupling due to similar charge density distributions of occupied and empty states.

Discussion

In this work, we used the ADAQ high-throughput screening framework, along with hybrid DFT and TDDFT methods and QDET, to discover and characterize a promising NV$^-$ spin defect in MgO. The oxide host satisfies all the desirable criteria listed in the seminal paper by Weber et al.[72]: it has a wide band gap, small spin-orbit coupling, it is available as high-quality thin films and bulk crystals, and both Mg and O have naturally occurring isotopes of zero nuclear spin and thus can be isotopically purified. Additionally, the recent study by Kanai et al.[5] predicted a single spin in MgO to have a coherence time (T_2) of 0.60 ms. This is slightly lower than the T_2 in prototypical hosts like diamond (0.89 ms) or SiC (1.1 ms) (primarily due to the larger concentration of nuclear spin isotopes of Mg). However, MgO could still be a promising host due to other advantages, particularly the ability to be grown as a high quality thin film via multiple routes[17,18], and its use in a wide range of applications. These include MgO tunnel barriers in spintronics devices[73], MgO buffer layers in superconducting[21] and ferroelectric[19,20] devices, and MgO heterogeneous catalyst support materials[74].

In addition to the favorable properties of the host, many properties of the NV$^-$ defect in MgO are promising as well. In particular, its spin triplet ground state provides a two-level system ($m_s = 0$ and $m_s = \pm 1$), and the large ZFS can enable isolation of the two sublevels. The large ZFS and generally low hyperfine interaction parameters could be beneficial to increase the coherence time of the defect compared to the estimate obtained by considering a single electron spin in MgO. The singlet states between the $^3A_2$ ground and first ^3E excited state, as determined using TDDFT-DDH and QDET (see Fig. 3b), can act as shelving states, thereby enabling optical initialization and spin sublevel-dependent photo-luminescence. The absence of crossing (or near-degeneracy) between the potential energy surfaces of the singlet and triplet states is an important indicator of the possibility of optical initialization and readout. The presence of singlet shelving states can also enable additional readout modes, for example spin-to-photocurrent (or spin-to-charge) readout. The efficiency of the initialization and optical read-out will depend on the radiative and non-radiative (ISC) transition rates. The transverse spin-orbit coupling component (which couples only the $m_s = \pm 1$ sublevels of ^3E to the singlet states) and the likely large vibrational overlap between ^3E and the singlet states, and between $^1B_1/^1B_2$ and the $^3A_2$ ground state, may lead to spin-sublevel selective depopulation of ^3E and efficient optical polarization. However, spin-dependent optical readout might be challenging: the near-degeneracy of the $^1A_1$ and ^3E states seen in Fig. 3c could lead to a much faster ISC rate between ^3E and $^1A_1$, compared to the radiative rate between ^3E and $^3A_2$, leading to poor spin-dependent optical readout contrast. The ISC rate could be reduced by applying strain to increase the energy spacing between the ^3E and $^1A_1$; note that even meV changes could lead to changes in the ISC rates. The role of the ISC between ^3E and $^1B_2$ or $^1B_1$ would also need to be clarified to obtain a complete picture of the optical cycle, and robust conclusions on the efficiency of optical read-out, will require the calculation of rates, which will be the subject of a future study. We emphasize that a favorable feature of the NV$^-$ defect in MgO is its emission in the visible red-infrared regime, making the experimental detection of this defect relatively straightforward. It is unlikely that the emitted light will be reabsorbed, as one may expect oxygen vacancies to be the additional most likely defect to be present in the oxide, and its photoexcitation and photoionization energies are around 5 eV[75]. The broad emission line-width of the NV$^-$ center may allow filtering of any emitted light from underlying substrates, while still retaining a substantial portion of emitted light from the defect which can be detected. Moreover, recent work on Er^{3+}-doped MgO[64] has demonstrated the integration of MgO with silicon nanophotonic cavities to achieve a cavity enhancement of over three orders of magnitude. This points to the promising possibility of using cavity enhancement of the optical transitions in the NV$^-$ center as well. Importantly, MgO can be doped with nitrogen, as demonstrated in previous experimental studies[29–34]. The hyperfine interaction parameters of the NV$^-$ center are different from those of other nitrogen-related defects, e.g. the nitrogen interstitial and nitrogen substitutional on the oxygen site[39], indicating that the NV$^-$ center should be experimentally distinguishable.

The properties of the NV$^-$ spin defect computed here and the wide technological applicability of MgO thin films point at applications that could integrate ‘classical’ spintronics and ferroelectrics with quantum information science. For example, classical information, e.g. magnetization direction in a magnetic tunnel junction (MTJ), with MgO as the tunnel barrier, can be mapped onto the spin defect, as it has been recently proposed by Jansen and Yuasa[76] in the case of a quantum dot. The NV$^-$ defect could also be used in conjunction with MgO MTJ-based nanomagnets to realize single qubit gates for quantum computing[77]. Similarly, it may be interesting to explore mapping of the polarization state of a ferroelectric thin film to control qubit interactions in MgO buffer layers[78–80]. Further, the properties of the NV$^-$ in MgO could make it a viable quantum sensor. In fact, flexible and wearable spintronic devices based on MgO-barrier MTJs have been recently developed[81]: combining the NV$^-$ spin defect with these devices could enable wearable quantum sensing.

A key challenge with the promising defect identified in our study is the strong vibronic coupling, which leads to a large ΔQ and consequently large HRF and low DWF, leading to an undetectable ZPL. This likely makes the NV$^-$ center in MgO unsuitable for quantum communication; however, quantum sensing and computing could be viable applications. Our study revealed that strain could help increase the DWF, however, one would need to go to extremely large strains to achieve a detectable ZPL. Note that the DWF can be increased via the formation of point-planar defect complexes, like in SiC nanowires, where complexes formed between point defects and stacking faults were found to have high brightness and DWF ≈ 50%.[59]. It is important to note that the large ΔQ and resulting low DWF found in our study at zero temperature represents the worst-case scenario, since all our analysis was done starting from a highly symmetric ground state structure. However, the NV$^-$ defect in MgO has multiple nearly-degenerate local minima with lower symmetry. Given that zero-point vibrational energy in MgO is non-negligible (it leads to a lattice constant expansion by 0.5% and bandgap renormalization by 6%[82,83]), it is likely that the zero-point vibrational energy will lead to symmetry breaking, which will reduce ΔQ and increase the DWF. Indeed, if we consider structures with broken symmetry in the ground state (as reported in our ADAQ search, see Supplementary Table 1), we find a decrease of the ΔQ.

Importantly, our study was able to shed light onto the reasons behind the strong vibronic coupling found for the NV$^-$ in MgO. Our APES analysis showed that the strong vibronic coupling is due to the large pJT stabilization energy in combination with the low effective phonon frequency along the symmetry-breaking e-phonon modes. This finding gives insight into design principles that could be considered while exploring or screening new spin defects, especially for enhancing optical addressability and/or enabling quantum communication applications. In particular, the strength of the vibronic coupling due to the pJT effect increases when the energy separation between excited states decreases[56]. This behavior is often correlated with the energy separation between the single-particle Kohn-Sham defect levels. Thus, to lower the vibronic coupling (therefore lowering ΔQ and HRF), the localized mid-gap states (both occupied and unoccupied) must be well-separated from each other, which is what we observe in substitutional complexes such as the $\mathrm{Al_{Mg}} - \mathrm{Al_O}$ defect in MgO (compare Fig. 5b with Fig. 2b for the NV$^-$). Moreover, the HRF increases when the charge distribution in the ground and excited state differ substantially in localization[55], which is the case for the NV$^-$ defect in MgO (where the excitation is from the O $2p$ defect states around the magnesium vacancy to the π-orbital around the N-O bond). Instead, in VV^0 in SiC, NV$^-$ in diamond, and even in the $\mathrm{Al_{Mg}} - \mathrm{Al_O}$ defect in MgO, the ground- and excited-state orbitals are localized in the same region of space. Thus, we expect spin defects in oxides comprising substitutional defects (including d- and f-dopants) to have lower vibronic coupling, leading to lower ΔQ and increased DWF. Moreover, our study shows that ΔQ, the separation between Kohn-Sham levels, and the localization of the electronic states involved in the excitation are good descriptors for screening or designing spin defects.

In sum, the computational protocol utilized in our study, combining high-throughput techniques and accurate electronic structure methods, helped identify and characterize a promising NV$^-$ defect in MgO. This new spin defect in a technologically mature material may be integrated into spintronic/ferroelectric applications to realize multifunctional electronics, including spintronic quantum logic gates and sensors. Overall, our results on the vibronic coupling of the NV$^-$ defect in MgO also contribute to the understanding of oxides as hosts for spin defects.

Methods

ADAQ

We used the ADAQ[22,23] software package and the high-throughput toolkit[24] to create and screen defects in MgO, and the automatic screening workflow is presented in ref. 22.

The MgO lattice parameter was optimized with the Perdew, Burke, and Erzenerhof (PBE) functional[84], and we obtained 4.25 Å. We used supercells with 512 atoms for all the defect calculations and the Lany-Zunger charge correction[85] with a dielectric constant $\epsilon_0 = 9.65$. In ADAQ, the calculations were performed with the Vienna Ab initio Simulation Package (VASP)[86,87], gamma compiled version 5.4.4, which uses the projector augmented wave (PAW)[88,89] pseudopotential (folder dated 2015-09-21). We used a plane-wave energy cutoff of 600 eV and kinetic energy cutoff of 900 eV for the augmentation charges, a total energy criterion of 10^{-4} eV, and a structural minimization criterion of 5×10^{-3} eV. Calculations were done at the Γ point. All the 2917 defects screened can be found in the ADAQ database online.

Electronic structure calculations

Once the NV$^-$- center was identified through the ADAQ procedure, we computed its ground state properties at the DFT level using Quantum ESPRESSO[90–92]. We used scalar-relativistic SG15 ONCV pseudopotentials (v. 1.2)[93,94] and the dielectric-dependent hybrid (DDH)[42] exchange-correlation functional, with a plane-wave cutoff of 80 Ry. Convergence tests for the plane-wave cutoff energy are provided in Supplementary Note 10. The inverse of the experimental macroscopic dielectric constant ϵ_∞ was used to determine the fraction of exact exchange α ($\epsilon_\infty = 2.96$[42,43], yielding $\alpha = \epsilon_\infty^{-1} = 0.34$). Given the computational cost of hybrid functionals, we used supercells with 216 atoms and we fixed the lattice constant to the experimental value extrapolated to 0 K, including the correction for zero-point anharmonic expansion effects[42] ($a_0 = 4.19$ Å). Note that this closely matches the DDH optimized lattice parameter (4.195 Å) as obtained from an equation-of-state fit (see Supplementary Note 11). The supercell Brillouin zone was sampled with the Γ point. Forces were converged to 0.01 eV/Å, and all calculations were spin-polarized.

We calculated the formation energy $E^f[D^q]$ of defect D in charge state q as[95]

$$E^f[D^q] = E_{tot}[D^q] - E_{tot}[bulk] - \sum_i n_i\mu_i + q(\varepsilon_f + E_{VBM}) + E_{corr} \tag{4}$$

where $E_{tot}[D^q]$ is the total energy of the supercell containing the defect D in charge state q, $E_{tot}[bulk]$ is the total energy of the pristine supercell of the same size, n_i is the number of atoms of species i added to ($n_i > 0$) or removed from ($n_i < 0$) the supercell to create the defect, μ_i is the chemical potential of species i, ε_f is the Fermi energy relative to the valence band maximum E_{VBM}, and E_{corr} is a charge-dependent term that corrects for artificial electrostatic interactions arising due to the finite size of the supercell and was calculated using the Freysoldt-Neugebauer-Van de Walle correction scheme[96] with the static dielectric constant for MgO $\epsilon_0 = 9.8$ taken from experiment[97]. Note that a comparison between the Lany-Zunger and Freysoldt-Neugebauer-Van de Walle correction schemes in the case of CaO[6] yielded very similar and fully consistent results, and we expect the same for MgO. The chemical potentials of oxygen, nitrogen, and magnesium were calculated as $\mu_O = \frac{1}{2}E_{DFT,O_2}$, $\mu_N = \frac{1}{2}E_{DFT,N_2}$, $\mu_{Mg} = E_{DFT,MgO} - \mu_O$. We used the HSE functional[98] to obtain E_{DFT,O_2} and E_{DFT,N_2}, as the binding energy and the bond length of the respective molecules calculated using the HSE functional matched more closely with experiments. Additional details can be found in Supplementary Note 12. A comparison of the defect formation energies computed at the PBE (the functional used in the ADAQ screening procedure) and DDH levels of theory is given in the Supplementary Information as well (Supplementary Note 13).

We computed the excited state properties, including the low-lying triplet and singlet states, and we optimized the geometry of the first excited triplet state using time-dependent DFT (TDDFT) under the Tamm-Dancoff approximation, the DDH functional and the WEST code[51,99,100]. Due to the higher computational cost of TDDFT calculations, the plane-wave cutoff was reduced to 60 Ry. Forces were converged to 0.01 eV/Å.

Vertical excitation energies and the resulting many-body electronic structure were also computed using the quantum defect embedding theory (QDET) with exact double counting corrections[52–54], using the WEST code[99,100]. The active space consisted of the localized defect orbitals (b_1, a_1, e_x, e_y) within the band gap as well as of several orbitals below the valence band maximum. We checked the convergence of the excitation energies by gradually increasing the number of orbitals below the valence band maximum (VBM) included in the active space, and found that convergence was achieved upon including orbitals up to 0.7 eV below the VBM. We note that in QDET with exact double counting correction, the environment is described using G_0W_0. In the WEST code, a separable form of W_0 is obtained using a technique called the projective eigendecomposition of the dielectric screening (PDEP), which avoids the inversion and storage of large dielectric matrices and enables the calculation of the self-energy matrix elements without explicitly evaluating empty states. The number of PDEP eigenpotentials used to obtain the separable form of W_0 was determined after convergence tests of the excitation energies as a function of the number of eigenpotentials. The active space Hamiltonian was solved exactly using the full-configuration interaction method implemented in pySCF[101,102]. Note that the electronic structure on which G_0W_0 and subsequent QDET calculations are based upon, was obtained by non-polarized DFT calculations.

The zero field splitting tensor was calculated using the GPU-accelerated version of pyZFS[103], considering spin-spin interactions and using wavefunctions from a DFT calculation of a 4 × 4 x 4 (3 × 3 x 3) supercell with the PBE (DDH) exchange-correlation functional.

Hyperfine interaction parameters were calculated using the gauge-including projector-augmented wave (GIPAW) method with core polarization effects as implemented in the GIPAW module[104] of Quantum ESPRESSO. Wavefunctions from a DFT calculation of a 4 × 4 x 4 supercell with the PBE exchange-correlation functional were used.

Configuration coordinate diagrams and emission spectra

The one-dimensional configuration coordinate diagrams (CCD) were constructed by linearly interpolating the coordinates between the optimized $^3A_2$ ground state and first ^3E excited state structures and performing single point DFT and TDDFT calculations for each point along the ground and excited states respectively (using the DDH functional). The effective phonon frequencies in the ground and excited states ($\hbar\omega_g$ and $\hbar\omega_e$ respectively) were obtained by fitting a quadratic function around the points near the respective minima. The Huang-Rhys and Debye-Waller factors were computed using $\hbar\omega_g$, $\hbar\omega_e$, and ΔQ, using Eq. (1).

Using the parameters obtained from the CCD, the normalized emission intensity $L(\hbar\omega)$ under the Franck-Condon approximation was calculated as

$$\begin{aligned} L(\hbar\omega) \quad &= \quad C\omega^3 \sum_i \sum_j P_{ej}(T) |\langle \Theta_{ej} | \Theta_{gi} \rangle|^2 \\ &\quad \times \delta(E_{ZPL} + E_{ej} - E_{gi} - \hbar\omega) \end{aligned} \tag{5}$$

Here C is a normalization factor, which includes the electronic transition dipole moment and the refractive index of the material, $P_{ej}(T)$ is the thermal occupation factor of the excited state phonons with energy E_{ej}, T is the temperature, $|\Theta_{gi}\rangle$ ($\langle\Theta_{ej}|$) is the ith (jth) harmonic nuclear wave function of the system in the ground (excited) state with vibrational energy E_{gi} (E_{ej}), and E_{ZPL} is the zero phonon line energy. The vibrational energies in the nth ground and excited states are given as $E_{gi} = n\hbar\omega_g$ and $E_{ej} = n\hbar\omega_e$ respectively. E_{ZPL} is the energy difference between the optimized geometries of the excited and ground states. The Franck-Condon factors $|\langle\Theta_{ej}|\Theta_{gi}\rangle|^2$ were calculated using the recurrence method[105]. The δ function was replaced by a Gaussian with a broadening parameter of 25 meV.

To quantify the coupling to the e-phonon modes, we built a configuration coordinate diagram between the averaged structure of the four equivalent excited state minima and the optimized geometry of the first excited state. Using the averaged structure as the reference one eliminates the contribution of the a-phonon modes, which are not Jahn-Teller (JT) or pseudo-Jahn Teller (pJT) active. The effective phonon frequencies and vibronic coupling constants were obtained by fitting an adiabatic potential energy surface (APES) to the CCD of the first excited state following the adiabatic-to-diabatic transformation method of refs. 65,66 and including JT and pJT coupling terms up to the sixth order.

Data availability

For more information about the ADAQ database, see https://httk.org/adaq/. Data that support the findings of this study will be made available at https://qresp.org/.

Received: 30 July 2024; Accepted: 18 February 2025;

References

1. Rodgers, L. V. et al. Materials challenges for quantum technologies based on color centers in diamond. *MRS Bull.* **46**, 623 (2021).
2. Castelletto, S. & Boretti, A. Silicon carbide color centers for quantum applications. *J. Phys.: Photonics* **2**, 022001 (2020).
3. De Leon, N. P. et al. Materials challenges and opportunities for quantum computing hardware. *Science* **372**, eabb2823 (2021).
4. Harmon, K. et al. Designing silicon carbide heterostructures for quantum information science: challenges and opportunities. *Mater. Quantum Technol.* **2**, 023001 (2022).
5. Kanai, S. et al. Generalized scaling of spin qubit coherence in over 12,000 host materials. *Proc. Natl Acad. Sci.* **119**, e2121808119 (2022).
6. Davidsson, J., Onizhuk, M., Vorwerk, C. & Galli, G. Discovery of atomic clock-like spin defects in simple oxides from first principles. *Nat. Commun.* **15**, 4812 (2024).
7. Butler, W., Zhang, X.-G., Schulthess, T. & MacLaren, J. Spin-dependent tunneling conductance of fe| mgo| fe sandwiches. *Phys. Rev. B* **63**, 054416 (2001).
8. Mathon, J. & Umerski, A. Theory of tunneling magnetoresistance of an epitaxial fe/mgo/fe (001) junction. *Phys. Rev. B* **63**, 220403 (2001).
9. Yuasa, S., Nagahama, T., Fukushima, A., Suzuki, Y. & Ando, K. Giant room-temperature magnetoresistance in single-crystal fe/mgo/fe magnetic tunnel junctions. *Nat. Mater.* **3**, 868 (2004).
10. Parkin, S. S. et al. Giant tunnelling magnetoresistance at room temperature with mgo (100) tunnel barriers. *Nat. Mater.* **3**, 862 (2004).
11. Yuasa, S. & Djayaprawira, D. Giant tunnel magnetoresistance in magnetic tunnel junctions with a crystalline mgo (0 0 1) barrier. *J. Phys. D: Appl. Phys.* **40**, R337 (2007).
12. Jiang, X. et al. Highly spin-polarized room-temperature tunnel injector for semiconductor spintronics using mgo (100). *Phys. Rev. Lett.* **94**, 056601 (2005).
13. Kapilashrami, M. et al. Experimental evidence for ferromagnetism at room temperature in mgo thin films. *J. Phys.: Condens. Matter* **22**, 345004 (2010).
14. Li, J. et al. Origin of room temperature ferromagnetism in mgo films. *Appl. Phys. Lett.* **102**, 072406 (2013).
15. Singh, J. P. & Chae, K. H. d ferromagnetism of magnesium oxide. *Condens. Matter* **2**, 36 (2017).
16. Jiang, G. et al. Solution-processed high-k magnesium oxide dielectrics for low-voltage oxide thin-film transistors. *Appl. Phys. Lett.* **109**, 183508 (2016).
17. Płóciennik, P. et al. Optical properties of mgo thin films grown by laser ablation technique. *Opt. Quantum Electron.* **48**, 1 (2016).
18. Valanarasu, S. et al. Microstructural, optical and electrical properties of various time annealed spin coated mgo thin films. *J. Mater. Sci.: Mater. Electron.* **25**, 3846 (2014).
19. Basit, N. A., Kim, H. K. & Blachere, J. Growth of highly oriented pb (zr, ti) o 3 films on mgo-buffered oxidized si substrates and its application to ferroelectric nonvolatile memory field-effect transistors. *Appl. Phys. Lett.* **73**, 3941 (1998).
20. Murphy, T., Chen, D. & Phillips, J. Electronic properties of ferroelectric batio3/ mgo capacitors on gaas. *Appl. Phys. Lett.* **85**, 3208 (2004).
21. Groves, J. R. et al. Ion-beam assisted deposition of bi-axially aligned mgo template films for ybco coated conductors. *IEEE Trans. Appl. Supercond.* **9**, 1964 (1999).
22. Davidsson, J., Ivády, V., Armiento, R. & Abrikosov, I. A. Adaq: Automatic workflows for magneto-optical properties of point defects in semiconductors. *Comput. Phys. Commun.* **269**, 108091 (2021).
23. Adaq, https://httk.org/adaq/ (2022), accessed: 2022-04-04
24. Armiento, R. Database-Driven High-Throughput Calculations and Machine Learning Models for Materials Design, in *Machine Learning Meets Quantum Physics*, Lecture Notes in Physics, Vol. 968, edited by Schütt, K. T., Chmiela, S., von Lilienfeld, O. A., Tkatchenko, A., Tsuda, K., and Müller, K.-R. (Springer International Publishing, Cham, 2020)
25. Davidsson, J., Stenlund, W., Parackal, A. S., Armiento, R. & Abrikosov, I. A. Na in diamond: High spin defects revealed by the adaq high-throughput computational database. *npj Comput. Mater.* **10**, 109 (2024).
26. Davidsson, J. et al. Exhaustive characterization of modified si vacancies in 4h-sic. *Nanophotonics* **11**, 4565 (2022).
27. El-Sayed, A.-M., Watkins, M. B., Grasser, T. & Shluger, A. L. Effect of electric field on migration of defects in oxides: Vacancies and interstitials in bulk mgo. *Phys. Rev. B* **98**, 064102 (2018).
28. Brudevoll, T., Kotomin, E. & Christensen, N. Interstitial-oxygen-atom diffusion in mgo. *Phys. Rev. B* **53**, 7731 (1996).
29. Yang, C.-H., *Ferromagnetism and Resisitive Switching in Magnesium Oxide with Nitrogen Doping* (Stanford University, 2010)
30. Liu, C.-M. et al. Optical and magnetic properties of nitrogen ion implanted mgo single crystal. *Chin. Phys. B* **20**, 047505 (2011).
31. Li, Q. et al. Room-temperature ferromagnetism observed in c-/n-/o-implanted mgo single crystals. *Chem. Phys. Lett.* **556**, 237 (2013).
32. Wang, X., Ma, C., Wang, X., Zhou, W. & Tan, W. Room temperature ferromagnetism in n-implanted mgo: Synergistic effects of intrinsic and extrinsic defects. *Mater. Res. Express* **8**, 066102 (2021).
33. Grob, M., Pratzer, M., Morgenstern, M. & Ležaić, M. Catalytic growth of n-doped mgo on mo (001). *Phys. Rev. B* **86**, 075455 (2012).
34. Li, Q. et al. Annealing temperature effects on the magnetic properties and induced defects in c/n/o implanted mgo. *Nucl. Instrum. Methods Phys. Res. Sect. B: Beam Interact. Mater. At.* **297**, 29 (2013).
35. Zhang, Y.-F., Liu, H., Wu, J. & Zuo, X. Ab initio study on nitrogen or carbon doped magnesium oxide. *IEEE Trans. Magn.* **47**, 2928 (2011).
36. Slipukhina, I., Mavropoulos, P., Blügel, S. & Ležaić, M. Ferromagnetic spin coupling of 2 p impurities in band insulators stabilized by an intersite coulomb interaction: Nitrogen-doped mgo. *Phys. Rev. Lett.* **107**, 137203 (2011).
37. Mavropoulos, P., Ležaić, M. & Blügel, S. Ferromagnetism in nitrogen-doped mgo: Density-functional calculations. *Phys. Rev. B* **80**, 184403 (2009).
38. Pardo, V. & Pickett, W. Magnetism from 2 p states in alkaline earth monoxides: Trends with varying n impurity concentration. *Phys. Rev. B* **78**, 134427 (2008).
39. Pesci, M., Gallino, F., Di Valentin, C. & Pacchioni, G. Nature of defect states in nitrogen-doped mgo. *J. Phys. Chem. C.* **114**, 1350 (2010).
40. Polfus, J. M., Bjørheim, T. S., Norby, T. & Haugsrud, R. Nitrogen defects in wide band gap oxides: defect equilibria and electronic structure from first principles calculations. *Phys. Chem. Chem. Phys.* **14**, 11808 (2012).
41. Bannikov, V., Shein, I. & Ivanovskii, A. Novel magnetic half-metallic materials based on ionic insulators doped with nonmagnetic impurities: Mgo+ b, c, n systems. *Tech. Phys. Lett.* **33**, 541 (2007).
42. Skone, J. H., Govoni, M. & Galli, G. Self-consistent hybrid functional for condensed systems. *Phys. Rev. B* **89**, 195112 (2014).
43. Lide, D. R., *CRC handbook of chemistry and physics*, Vol. 85 (CRC press, 2004)
44. Hong, C.-R., Yoon, S.-H. & Kim, Y.-S. Effects of exo-electron emission from mgo thin film on statistical delay of glow discharge of ac-pdp. *Thin Solid Films* **517**, 4170 (2009).

45. Perez, A., Marest, G., Sawicka, B., Sawicki, J. & Tyliszczak, T. Iron-ion—implantation effects in mgo crystals. *Phys. Rev. B* **28**, 1227 (1983).
46. Van de Walle, C. G. & Neugebauer, J. First-principles calculations for defects and impurities: Applications to iii-nitrides. *J. Appl. Phys.* **95**, 3851 (2004).
47. Seo, H., Ma, H., Govoni, M. & Galli, G. Designing defect-based qubit candidates in wide-gap binary semiconductors for solid-state quantum technologies. *Phys. Rev. Mater.* **1**, 075002 (2017).
48. Smart, T. J., Li, K., Xu, J. & Ping, Y. Intersystem crossing and exciton–defect coupling of spin defects in hexagonal boron nitride. *npj Comput. Mater.* **7**, 59 (2021).
49. Meesala, S. et al. Strain engineering of the silicon-vacancy center in diamond. *Phys. Rev. B* **97**, 205444 (2018).
50. Schulte, K. A., Vignesh, K. R. & Dunbar, K. R. Effects of coordination sphere on unusually large zero field splitting and slow magnetic relaxation in trigonally symmetric molecules. *Chem. Sci.* **9**, 9018 (2018).
51. Jin, Y., Yu, V. W.-z, Govoni, M., Xu, A. C. & Galli, G. Excited state properties of point defects in semiconductors and insulators investigated with time-dependent density functional theory. *J. Chem. Theory Comput.* **19**, 8689 (2023).
52. Ma, H., Sheng, N., Govoni, M. & Galli, G. Quantum embedding theory for strongly correlated states in materials. *J. Chem. Theory Comput.* **17**, 2116 (2021).
53. Sheng, N., Vorwerk, C., Govoni, M. & Galli, G. Green's function formulation of quantum defect embedding theory. *J. Chem. Theory Comput.* **18**, 3512 (2022).
54. Vorwerk, C., Sheng, N., Govoni, M., Huang, B. & Galli, G. Quantum embedding theories to simulate condensed systems on quantum computers. *Nat. Comput. Sci.* **2**, 424 (2022).
55. Stoneham, A. M., *Theory of defects in solids: electronic structure of defects in insulators and semiconductors* (Oxford University Press, 2001).
56. Bersuker, I. *The Jahn-Teller Effect* (Cambridge University Press, 2006).
57. Jin, Y. et al. Photoluminescence spectra of point defects in semiconductors: Validation of first-principles calculations. *Phys. Rev. Mater.* **5**, 084603 (2021).
58. Alkauskas, A., Buckley, B. B., Awschalom, D. D. & Van de Walle, C. G. First-principles theory of the luminescence lineshape for the triplet transition in diamond nv centres. *N. J. Phys.* **16**, 073026 (2014).
59. Lee, J. H. et al. Strong zero-phonon transition from point defect-stacking fault complexes in silicon carbide nanowires. *Nano Lett.* **21**, 9187 (2021).
60. Gali, Á. Ab initio theory of the nitrogen-vacancy center in diamond. *Nanophotonics* **8**, 1907 (2019).
61. Bian, G., Thiering, G. & Gali, Á. Theory of optical spinpolarization of axial divacancy and nitrogen-vacancy defects in 4h-sic, arXiv preprint arXiv:2409.10233 (2024)
62. Lee, Y. et al. Spin-defect qubits in two-dimensional transition metal dichalcogenides operating at telecom wavelengths. *Nat. Commun.* **13**, 7501 (2022).
63. Turiansky, M. E., Parto, K., Moody, G. & Van de Walle, C. G. Rational design of efficient defect-based quantum emitters. *APL Photonics* **9**, 066117 (2024)
64. Horvath, S. P. et al. Strong purcell enhancement of an optical magnetic dipole transition arXiv preprint arXiv:2307.03022 (2023)
65. Viel, A. & Eisfeld, W. Effects of higher order jahn-teller coupling on the nuclear dynamics. *J. Chem. Phys.* **120**, 4603 (2004).
66. Eisfeld, W. & Viel, A. Higher order (a+ e) ⊗ e pseudo-jahn–teller coupling. *J. Chem. Phys.* **122**, 204317 (2005).
67. Jin, Y., Govoni, M. & Galli, G. Vibrationally resolved optical excitations of the nitrogen-vacancy center in diamond. *npj Comput. Mater.* **8**, 238 (2022).
68. Karin, T., Dunham, S. & Fu, K.-M. Alignment of the diamond nitrogen vacancy center by strain engineering. *Appl. Phys. Lett.* **105**, 053106 (2014).
69. Seo, H., Govoni, M. & Galli, G. Design of defect spins in piezoelectric aluminum nitride for solid-state hybrid quantum technologies. *Sci. Rep.* **6**, 20803 (2016).
70. Vassent, J., Dynna, M., Marty, A., Gilles, B. & Patrat, G. A study of growth and the relaxation of elastic strain in mgo on fe (001). *J. Appl. Phys.* **80**, 5727 (1996).
71. Valeri, S. et al. Thickness-dependent strain in epitaxial mgo layers on ag (001). *Surf. Sci.* **507**, 311 (2002).
72. Weber, J. et al. Quantum computing with defects. *Proc. Natl Acad. Sci.* **107**, 8513 (2010).
73. Dieny, B. et al. Opportunities and challenges for spintronics in the microelectronics industry. *Nat. Electron.* **3**, 446 (2020).
74. Julkapli, N. M. & Bagheri, S. Magnesium oxide as a heterogeneous catalyst support. *Rev. Inorg. Chem.* **36**, 1 (2016).
75. Vorwerk, C. & Galli, G. Disentangling photoexcitation and photoluminescence processes in defective mgo. *Phys. Rev. Mater.* **7**, 033801 (2023).
76. Jansen, R. & Yuasa, S. High temperature spin selectivity in a quantum dot qubit using reservoir spin accumulation. *npj Quantum Inf.* **10**, 21 (2024).
77. Niknam, M. et al. Quantum control of spin qubits using nanomagnets. *Commun. Phys.* **5**, 284 (2022).
78. Levy, J. Quantum-information processing with ferroelectrically coupled quantum dots. *Phys. Rev. A* **64**, 052306 (2001).
79. Liu, J. et al. Coherent electric field manipulation of fe3+ spins in pbtio3. *Sci. Adv.* **7**, eabf8103 (2021).
80. George, R. E., Edwards, J. P. & Ardavan, A. Coherent spin control by electrical manipulation of the magnetic anisotropy. *Phys. Rev. Lett.* **110**, 027601 (2013).
81. Chen, J.-Y., Lau, Y.-C., Coey, J., Li, M. & Wang, J.-P. High performance mgo-barrier magnetic tunnel junctions for flexible and wearable spintronic applications. *Sci. Rep.* **7**, 42001 (2017).
82. Schimka, L., Harl, J. & Kresse, G. Improved hybrid functional for solids: The HSESOL functional. *J. Chem. Phys.* **134**, 024116 (2011).
83. Wing, D. et al. Band gaps of crystalline solids from wannier-localization–based optimal tuning of a screened range-separated hybrid functional. *Proc. Natl Acad. Sci.* **118**, e2104556118 (2021).
84. Perdew, J. P., Burke, K. & Ernzerhof, M. Generalized gradient approximation made simple. *Phys. Rev. Lett.* **77**, 3865 (1996).
85. Lany, S. & Zunger, A. Assessment of correction methods for the band-gap problem and for finite-size effects in supercell defect calculations: Case studies for zno and gaas. *Phys. Rev. B* **78**, 235104 (2008).
86. Kresse, G. & Hafner, J. Ab initio molecular-dynamics simulation of the liquid-metal-amorphous-semiconductor transition in germanium. *Phys. Rev. B* **49**, 14251 (1994).
87. Kresse, G. & Furthmüller, J. Efficient iterative schemes for ab initio total-energy calculations using a plane-wave basis set. *Phys. Rev. B* **54**, 11169 (1996).
88. Blöchl, P. E. Projector augmented-wave method. *Phys. Rev. B* **50**, 17953 (1994).
89. Kresse, G. & Joubert, D. From ultrasoft pseudopotentials to the projector augmented-wave method. *Phys. Rev. B* **59**, 1758 (1999).
90. Giannozzi, P. et al. Advanced capabilities for materials modelling with quantum espresso. *J. Phys.: Condens. matter* **29**, 465901 (2017).
91. Giannozzi, P. et al. Quantum espresso: a modular and open-source software project for quantum simulations of materials. *J. Phys.: Condens. Matter* **21**, 395502 (2009).
92. Giannozzi, P. et al. Quantum espresso toward the exascale. *J. Chem. Phys.* **152**, 154105 (2020).
93. Hamann, D. Optimized norm-conserving vanderbilt pseudopotentials. *Phys. Rev. B* **88**, 085117 (2013).

94. Schlipf, M. & Gygi, F. Optimization algorithm for the generation of oncv pseudopotentials. *Computer Phys. Commun.* **196**, 36 (2015).
95. Freysoldt, C. et al. First-principles calculations for point defects in solids. *Rev. Mod. Phys.* **86**, 253 (2014).
96. Freysoldt, C., Neugebauer, J. & Van de Walle, C. G. Fully ab initio finite-size corrections for charged-defect supercell calculations. *Phys. Rev. Lett.* **102**, 016402 (2009).
97. Subramanian, M., Shannon, R., Chai, B., Abraham, M. & Wintersgill, M. Dielectric constants of beo, mgo, and cao using the two-terminal method. *Phys. Chem. Miner.* **16**, 741 (1989).
98. Krukau, A. V., Vydrov, O. A., Izmaylov, A. F. & Scuseria, G. E. Influence of the exchange screening parameter on the performance of screened hybrid functionals. *J. Chem. Phys.* **125**, 224106 (2006).
99. Govoni, M. & Galli, G. Large scale gw calculations. *J. Chem. theory Comput.* **11**, 2680 (2015).
100. Yu, V. W.-z & Govoni, M. Gpu acceleration of large-scale full-frequency gw calculations. *J. Chem. Theory Comput.* **18**, 4690 (2022).
101. Sun, Q. et al. Pyscf: the python-based simulations of chemistry framework. *Wiley Interdiscip. Rev.: Comput. Mol. Sci.* **8**, e1340 (2018).
102. Sun, Q. et al. Recent developments in the pyscf program package. *J. Chem. Phys.* **153**, 024109 (2020).
103. Ma, H., Govoni, M. & Galli, G. Pyzfs: A python package for first-principles calculations of zero-field splitting tensors. *J. Open Source Softw.* **5**, 2160 (2020).
104. Varini, N., Ceresoli, D., Martin-Samos, L., Girotto, I. & Cavazzoni, C. Enhancement of dft-calculations at petascale: nuclear magnetic resonance, hybrid density functional theory and car–parrinello calculations. *Comput. Phys. Commun.* **184**, 1827 (2013).
105. Ruhoff, P. T. Recursion relations for multi-dimensional franck-condon overlap integrals. *Chem. Phys.* **186**, 355 (1994).
106. Gali, A., Janzén, E., Deák, P., Kresse, G. & Kaxiras, E. Theory of spin-conserving excitation of the n- v- center in diamond. *Phys. Rev. Lett.* **103**, 186404 (2009).
107. Gordon, L., Janotti, A. & Van de Walle, C. G. Defects as qubits in 3 c- and 4 h- sic. *Phys. Rev. B* **92**, 045208 (2015).

Acknowledgements

We thank Dr. F. Joseph Heremans, Prof. Shun Kanai, and Dr. Christian Vorwerk for many useful discussions. V.S acknowledges the support from the Maria Goeppert Mayer Named Fellowship, under the Laboratory Directed Research and Development (LDRD) funding from Argonne National Laboratory, provided by the Director, Office of Science, of the U.S. Department of Energy under Contract No. DE-AC02-06CH11357. J.D. acknowledges support from the Swedish e-science Research Centre (SeRC), the Knut and Alice Wallenberg Foundation through the WBSQD2 project (Grant No. 2018.0071), and the Swedish Research Council (VR) Grant No. 2022-00276. This work was supported by the Air Force Office of Scientific Research (AFOSR) through the CFIRE grant # FA95502310667. This work used several codes, including the WEST code whose development is supported by MICCoM, which is part of the Computational Materials Sciences Program funded by the U.S. Department of Energy, Office of Science, Basic Energy Sciences, Materials Sciences, and Engineering Division through Argonne National Laboratory. This research used resources of the National Energy Research Scientific Computing Center (NERSC), a Department of Energy Office of Science User Facility using NERSC award DDR-ERCAP0029604, resources of the University of Chicago Research Computing Center, and resources of the Argonne Leadership Computing Facility, a U.S. Department of Energy (DOE) Office of Science user facility at Argonne National Laboratory, which is supported by the Office of Science of the U.S. DOE under Contract No. DE-AC02-06CH11357. The ADAQ computations were enabled by resources provided by the National Academic Infrastructure for Supercomputing in Sweden (NAISS) at the Swedish National Infrastructure for Computing (SNIC) at Tetralith, partially funded by the Swedish Research Council through grant agreement no. 2022-06725.

Author contributions

V.S.: calculations and analyses; J.D.: ADAQ methodology and high-throughput screening; Y.J.: TDDFT and PL methodology; G.G.: designed and supervised the research. V.S. and G.G. wrote the manuscript. All authors contributed to discussions and finalizing the manuscript.

Competing interests

The authors declare no competing interests.

Additional information

Supplementary information The online version contains supplementary material available at https://doi.org/10.1038/s41524-025-01558-w.

Correspondence and requests for materials should be addressed to Giulia Galli.